

Broadband Plasmonic Photocatalysis Enhanced by Photothermal Light Absorbers

Zhijia Geng, Yifan Yu, Jie Liu*

Department of Chemistry, Duke University, Durham, North Carolina 27708, United States.

ABSTRACT

Plasmonic photocatalysis is an emerging research field that holds promise for sustainable energy applications, particularly in solar energy conversion. In this study, we focus on the enhancement of broadband light absorption capabilities for plasmonic photocatalyst under white light illumination. By replacing parts of the catalyst with solar absorber, we can significantly improve the total reaction rate under mild heating conditions with less catalyst. Through careful comparison of reaction conditions and systematic optimization of the contributions from photothermal and non-thermal effects, we demonstrate a substantial enhancement in broadband light absorption capacity and overall light effectiveness, paving the way for advanced plasmonic photocatalysts with greater efficiency and practical applicability using solar light as the energy source.

INTRODUCTION

With the rapid depletion of fossil fuels and the projected doubling of global energy demand by the mid-century, there is an urgent need for alternative energy sources.¹ In recent years, solar radiation has emerged as a promising and sustainable solution, offering a reliable substitute to traditional fossil fuels. Solar energy harnesses the vast and clean power of the sun, providing a renewable and environmentally friendly source of electricity generation.² The efficiency of converting solar radiation into usable heat critically depends on the absorptivity of a solar thermal collector, thus emphasizing the pivotal role of the solar absorber in the solar thermal systems. Since approximately 95% of solar radiation falls within the wavelength range of 0.3 to 2.0 μm , spanning from UV to NIR, it becomes imperative for the material surface to exhibit optimal optical absorption in the visible and near-infrared (IR) spectral range. Some common used light absorbers are plasmonic nanoparticles (Au³⁻⁶, Ag⁷⁻⁹, Pd^{10, 11}), semiconductors (Cu_{2-x}S^{12, 13}, Ti₂O₃^{14, 15}, Fe₃O₄¹⁶), carbon based materials^{17, 18} and polymers^{19, 20}. While these solar absorbers have found effective in water desalination and evaporation²¹⁻²⁴ and water splitting^{25, 26}, their utilization in gas phase reactions, such as photocatalytic CO₂ reduction, which is crucial for solar-to-fuel conversion and energy storage, remains less explored.^{27, 28}

For traditional photocatalytic reaction, semiconductor such as TiO₂ has shown to be a good support for gaseous reactions.²⁹⁻³¹ Limited by the poor absorption of photons under visible light and fast recombination rate between generated electron-hole pairs, semiconductors could overcome these disadvantages by adding the metal nanoparticles (NPs) as co-catalysts to improve the catalytic performance.³² Plasmonic metal nanoparticles exhibit localized surface plasmon resonance (LSPR), generating high-energy electrons or holes upon resonance wavelength excitation. The chemical reactions of adsorbates, triggered by high-energy electrons or holes generated from the decay of LSPR, either through electron or vibrational excitation, represent widely accepted mechanisms in plasmon-induced photochemistry.³³ Experimental evidence has shown that hot

carriers (HC) can effectively lower activation barriers and facilitate molecular rearrangement.^{34, 35} Given that the bandgap of TiO₂ is approximately 3.2 eV, requiring ultraviolet (UV) radiation with wavelengths shorter than 385 nm, photocatalysis with TiO₂ utilizes only less than 5% of the energy available in sunlight. By introducing plasmonic NPs, like Au^{32, 36}, Ag^{37, 38}, Cu^{39, 40}, Al^{41, 42}, and Rh NPs^{43, 44} enhanced productivity, selectivity and absorption in the UV to visible range can be achieved. Rh/TiO₂ was used as plasmonic photocatalyst since it showed great production rate and high selectivity towards CH₄ under mild thermal conditions in CO₂ reduction reaction.^{43, 45, 46}

Despite its promise, the research field of plasmonic catalysis remains encumbered by several challenges and ongoing debates.⁴⁷ One such ongoing debate build around the relative significance between photothermal and non-thermal effects. Distinguishing between these two effects in plasmonic catalysis is crucial for deciphering the underlying reaction mechanisms. Previous studies have indicated that certain reactions are primarily driven by photothermal effects⁴⁸, while others depend more on non-thermal effects.^{49, 50} However, only a handful of investigations have sought to exploit the synergistic relationship between these thermal and non-thermal influences.^{32, 51} From a practical application perspective, the ultimate enhanced production rate and effective utilization of light are desired. However in current plasmonic photocatalysis, researchers are trying hard in quantitatively separate the thermal and non-thermal effects and trying to study the effects and mechanisms separately.^{34, 52, 53} By studying the synergetic effects from photothermal and non-thermal contributions, a better way of light utilization can be achieved.^{30, 43, 44, 54} Therefore, it is important to study how we could enhance the photothermal contribution to the reaction and the most effective way of combining them.

Furthermore, we have previously introduced a new index named as overall light effectiveness (OLE) to evaluate the combined photothermal and non-thermal effects. We reported that, using Rh/TiO₂ in CO₂ reduction, the highest OLE was achieved at 325 °C under 0.67 W·cm⁻² UV light (365 nm) irradiation. These results indicated that the highest light effectiveness can only be achieved by combining both photothermal and non-thermal effects. Therefore, in order to enhance the absorptivity of the catalyst under solar light and increase the contribution of photothermal effects towards higher OLE, here we propose an innovative method by mixing the plasmonic photocatalyst with the broad bandgap solar absorber to enhance the catalytic performance under milder heating conditions with white light illumination. One of the solar absorbers we studied is titanium nitride (TiN). TiN has previously shown to play a significant role in enhancing the solar absorptivity efficiency, and been used in multiple dielectric solar absorbers for solar energy harvesting.⁵⁵⁻⁵⁷ The main conclusion is that by mixing the solar absorber with plasmonic photocatalysis, the total production rate and OLE increased under milder heating environment with an extended absorption spectrum under white light illumination compared to UV light. Consequently, it is possible to design plasmonic catalysts that can utilize the energy from the full spectrum of sunlight for efficient enhancement of important chemical reactions, overcoming the limitation of traditional photocatalysis.

METHODS

Material synthesis. The catalyst synthesis process can be found in our previous publication.⁴³ In general, rhodium nanoparticles are prepared by a modified polyol method. Polyvinylpyrrolidone

(100 mg, PVP, Mw = 55,000, Aldrich) was dissolved in ethylene glycol (22.4 mL, EG, Fisher) in a 100 mL round bottom flask, and stirred in an oil bath with constant heating at 160 °C for 30 min. Rhodium (III) chloride hydrate (48 mg, $\text{RhCl}_3 \cdot \text{H}_2\text{O}$, 40% Rh, Pressure Chemical) was first dissolved in 1.6 mL EG in a separate viral and quickly injected into the hot solution. The reaction mixture was kept stirring for another 30 min, and then cooled to room temperature. The brownish solution of Rh nanospheres was washed with 20 mL acetone three times to remove the spectator ions. The residue was mixed with 3 mL of deionized water and 30 mL ethanol under sonication till fully dissolved. The oxide support, titanium dioxide (~ 380 mg, TiO_2 , Degussa, P25, specific surface area 35-65 $\text{m}^2 \cdot \text{g}^{-1}$), was activated in air at 500 °C for 5 h before impregnation. The pre-heated TiO_2 was added to nanoparticle solution and stirred vigorously overnight. The mixture was then dried on the hotplate till all the solvent evaporated. The remained solid was ground into a fine powder and calcined in air at 400 °C for 2h. The collected powder was stored in oven at 70 °C for further measurement.

Titanium nitride (TiN , 99.5%, metal basis, Thermo scientific) was used as received and mixed with Rh/TiO_2 to reach 4:1 ratio by mass. The mixture was grounded in a mortar and pestle set for 30 minutes to get an even mixing. The powder was then collected and stored for measurements.

CO₂ reduction and product analysis. All data shown in this work is obtained using a system consisting of a gas delivery system, a fixed-bed reactor equipped with a quartz window, LED/laser light sources ((Prizmatix, UHP-F, 365 nm), an online mass spectrometer, and a multi-thermocouple setup with a programmable temperature controller. The catalysts are placed inside the Harrick reactor, and thermocouples (TCs) are used for temperature measurements. There is a total of 3 TCs that have been placed inside the reactor, and any one of the TC can be selected to maintain the set temperature and monitored by a PID temperature controller kit (Harrick, ATK-024-3). The surface TC (TC1) is the one that being placed nearest to the top surface of the catalyst layer. The collected temperature is expected to be the real surface temperature. The bottom TC (TC2) measures the temperature at the lower part of the catalyst. The heater TC (TC3) is placed right above the heating cable and is supposed to record the temperature from the cable heater. T3 is selected as the reference TC for controlling the PID output of the external heating, since it is buried deep inside the reactor and will endure the least amount of influences from light. Therefore, the external heating should be constant under the same set temperature. The other two TCs are connected with a handheld temperature data logger (Omega, RDXL6SD-USB) and used to record the real-time temperatures from two positions in the reaction chamber.

For each experiment, approximately 20 mg of the prepared Rh/TiO_2 catalyst and 5 mg TiN was loaded in the reactor to fill a 6-mm diameter, 3-mm height catalyst cup (stainless steel, 500 mesh, 0.0010") to ensure the complete absorption of light for the catalytic measurement. The $\text{Rh/TiO}_2:\text{TiN}$ photocatalysts were first reduced under 60 standard cubic centimeters per minute (sccm) H_2 and 40 sccm Ar at 350 °C for 2 h to remove any Rh oxidation, and then the gas flow was switched to a mixture of CO_2 , H_2 , and Ar with the desired ratio and a total flow rate of 60 sccm. The gaseous product was monitored by an inline quadrupole mass spectrometer (Hiden, HPR-20) equipped with a Faraday cup and secondary electron multiplier (SEM) detector at $\text{m/z} = 2$ (H_2), 15 (CH_4), 18 (H_2O), 28 (CO), 40 (Ar) and 44 (CO_2) in real time with filament settings of

70 V and 250 μ A. The detection limit of the mass spectrometer was $\sim 0.001\%$ conversion of CO₂. For each temperature and light intensity condition, at least 30 min elapsed before ten sequential measurements were made to ascertain the steady-state concentration of each gas and the associated reaction rates and uncertainties. All reactions were operated under atmospheric pressure. Mass spectrometer signals were calibrated using calibration gases (Gasco, Inc., 1 vol% CH₄/Ar) over a range of flow rates and with argon gas as an internal standard. For example, the CH₄ production rate was calculated according to Eq. (1).

$$R_{CH_4} (\mu\text{mol} \cdot \text{g}^{-1} \cdot \text{s}^{-1}) = \frac{\left(\text{flow } \frac{CH_4}{Ar} \text{ ratio} \right) (fAr, \text{sccm}) (10^6, \mu\text{mol} \cdot \text{mol}^{-1})}{(60, \text{s} \cdot \text{min}^{-1}) (22,400, \text{mL} \cdot \text{mol}^{-1}) (m_{\text{catalyst}}, \text{g})} \quad (1)$$

Characterization. Transmission electron microscopy (TEM) images were collected by an FEI Tecnai G2 Twin operating at 200 kV. The TEM samples were prepared by dispersing the Rh nanospheres and Rh photocatalysts in ethanol with sonication, then depositing on a copper grid coated with a carbon film (Ted Pella, 01813). Scanning electron microscopy (SEM) with energy dispersive X-ray spectroscopy (EDS) images were collected by a ThermoFisher Scientific Apreo 2 SEM. Diffuse reflectance UV-vis extinction spectra were obtained on an Agilent Cary 5000 equipped with an external diffuse reflectance accessory (DRA-2500). The composition of the photocatalysts was measured by a Kratos Analytical Axis Ultra X-ray photoelectron spectrometer (XPS).

RESULTS AND DISCUSSION

The TEM characterizations of both Rh/TiO₂ and Rh/TiO₂:TiN (4:1) is shown in Figure 1. As can be seen, after grinding TiN and Rh/TiO₂ for 30 min, they achieved an even mixture where large TiN particles are surrounded by Rh/TiO₂ (Figure 1b). The UV-Vis spectra of the studied materials show the enhanced absorption for Rh/TiO₂:TiN within the visible light region compared to Rh/TiO₂ (Figure 1c). For TiO₂, it shows the highest absorption peak under UV region, which is related to the band gap energy in the TiO₂ structure. Enhance absorption in the region of 400 – 800 nm, compared with pure P25 TiO₂ particles was observed with sample with Rh NP deposition. Rh NPs show a general size distribution around 5-6 nm (Figure S1, Supporting Information). Even though Rh NPs only generate LSPR effect under UV region, adding Rh NPs can still enhance the absorption under visible light (Figure S2a).⁵⁸ The inclusion of TiN further amplified the enhancement. Moreover, for comparison study, Rh/TiO₂:TiO₂ (4:1) was prepared through the same method. The UV-Vis spectrum shows no enhancement with the addition of TiO₂ onto Rh/TiO₂ (Figure S2b). XPS was employed to confirm the mix of Rh/TiO₂ and TiN as well. Due to the small portion of TiN, the N 1s peak (397 eV) is too weak to be shown in the survey XPS spectra of Rh/TiO₂:TiN (4:1) (Figure 1d). However, the Ti 2p XPS spectra indicate the existence of TiN (Figure 1e). There are two typical peaks at 456.0 and 457.7 eV, which represent the Ti-N bonds and the Ti-O bonds on the surface, respectively. Moreover, the XPS results showed that the Ti 2p remained unchanged and Rh 3d oxidize state reduced under H₂ reduction at 400 °C for 2 hours, indicating the primary role for H₂ reduction before experiment in removing the potential oxidized species on Rh NPs (Figure S3).

We then performed the catalytic studies using Rh/TiO₂ and Rh/TiO₂:solar absorber for CO₂ reduction reaction. The reaction studied here was CO₂ + H₂ → CH₄ + H₂O. The selectivity towards CH₄ under 400 °C heating and 1.4 W·cm⁻² UV light illumination was nearly 100% with trace amount of CO signal increment detected under higher thermal condition (Figure S4).⁴³ In general, 5 mg of TiO₂ was put under 20 mg of catalyst to support the catalyst and maintain the same surface level (Figure 2a). The addition of TiO₂ played a crucial role in maintaining the same distance between light source and catalyst surface to control the light effects. Several thermal couples were placed inside the reactor to record and control the temperature profile (Figure S5). The total production rate of methane was studied, and we conducted a screening of potential solar absorber combinations, like TiN, Ti₂O₃, Co₃O₄, CoWO₄, (Figure 2b) and with different ratios (1:1, 3:2, 4:1) (Figure 2c). The results showed that the addition of TiN as solar absorber in 4:1 ratio by mass can greatly enhance the photocatalytic performance of Rh/TiO₂ under 100 °C external heating with white light illumination.

Since Rh NP can only be LSPR excited under UV light, the catalyst would not generate non-thermal effect under white light.⁵⁸ Contrary to the addition of TiO₂, which can absorb UV light, replacing 20 % amount of Rh/TiO₂ into TiN would not decrease the production rate under light illumination, but increase the production rate by a factor of 1.26 due to the enhanced visible light absorption and increased photothermal contribution (Figure 3a). The result showed that the measured surface temperature by TC1 increased from 196 to 216 °C with addition of TiN under 100 °C heating and 1.9 W·cm⁻² white light illumination (Figure 3b). Similar increment in production rate was observed when the external heating increased to 325 °C under low light intensities (Figure 3c). As the light intensity increased from 0.7 to 1.9 W·cm⁻², the increment in total production rate dropped from 10% to nearly zero. With 0 W·cm⁻² light intensity, there was no light effect, and all the catalyst would undergo dark thermal heating mechanism. The results showed that both Rh/TiO₂:TiN (4:1) and Rh/TiO₂:TiO₂ (4:1), both containing 16 mg of catalyst, generated about 80% amount of product compared to 20 mg pure catalyst under dark condition. However, with the increase in light intensity, the photothermal effect from TiN leads to the increased production rates from 0.5 – 1.5 W·cm⁻² compared to the pure catalyst. These three catalysts ultimately reached to a similar production rate beyond 1.5 W·cm⁻², where the photothermal contribution approached to a limit, and the total production rates would not increase further with the changes in light intensity and surface temperature (Figure 3d). This trend indicated that as the external heating increased from 100 to 325 °C and light intensity from 0 to 1.9 W·cm⁻², the photothermal effect from the top of catalyst layer would contribute less to the total production rate, while the external thermal effect from the bottom dark catalyst contributed more. To eliminate the interference from solar absorbers towards the catalytic performance of the catalyst mixture, we performed the studies with TiN only. The results showed that TiN exhibits minimum photocatalytic and thermocatalytic performances under white light compared to Rh/TiO₂ (Figure S6a). Therefore, we were able to show that by replacing part of the catalyst as solar absorber, fewer amount of catalyst were used to achieve a better production rate due to the extra generated photothermal effects from the addition of solar absorbers.

After showing the enhancement in total production rate in a simpler system with only photothermal effect, we then performed the study to see how the extra photothermal effect could influence the plasmonic photocatalysis when performing the same reaction under UV light. The wavelength dependence study on TiN showed little difference between white light and UV under 325 °C (Figure S6b). Moreover, the studies on the catalytic performance of TiO₂ showed that under dark condition, TiO₂ as a porous material can help the methane production. The introduction of UV light did not influence the behavior, indicating the poor TiO₂ photocatalytic performance (Figure S7). Therefore, the catalytic effects from TiN and TiO₂ in Rh/TiO₂:TiN (4:1) could still be ignored.

Based on the performances of Rh/TiO₂, which is a well-studied UV-active plasmonic catalyst⁴³, the methane production was higher under UV than white with similar light intensities due to the existence of non-thermal effects generated from LSPR of Rh NP for 100 °C (Figure 4a). Additionally, the same reaction performed using Rh/TiO₂:TiN (4:1) showed a reverse trend, where the production rate was higher under white light (0.59 $\mu\text{mol}\cdot\text{s}^{-1}$) than UV (0.35 $\mu\text{mol}\cdot\text{s}^{-1}$) for 70 % with 100 °C heating and 1.4 W·cm⁻² light illumination, where the photothermal effect from TiN was dominant. We could then cross compared the catalytic behaviors between these two catalysts under same wavelength. Under 1.4W·cm⁻² UV light, the production rate was 0.31 $\mu\text{mol}\cdot\text{s}^{-1}$ for Rh/TiO₂ and 0.34 $\mu\text{mol}\cdot\text{s}^{-1}$ for Rh/TiO₂:TiN (4:1). Under 1.5 W·cm⁻² white light, the production rate was 0.31 $\mu\text{mol}\cdot\text{s}^{-1}$ for Rh/TiO₂ and 0.59 $\mu\text{mol}\cdot\text{s}^{-1}$ for Rh/TiO₂:TiN (4:1). The increases in production rate were 11% under UV light and 92% under white light with relatively similar light intensity, where the increases in surface temperature were the same after adding the solar absorber (Figure 4b). Similar trend could be seen from Rh/TiO₂ under 325 °C with an enhancement on production rate between UV and white between 0.5 – 1 W·cm⁻² due to the non-thermal effect (Figure 4c). However, the rate enhancement due to replacement was lower and nearly indistinguishable between UV and white light, when we increased the external heating to 325 °C, regardless the similar surface temperature increment by solar absorber (Figure 4d).

Under a mild heating condition, like 100 °C, the replacement of catalyst to TiN would the increase of photothermal effects but sacrificing the surface non-thermal contribution from Rh/TiO₂ under UV light. Clearly, the results illustrated that replacing the surface catalyst with solar absorber would bring more positive effects to the total production rate and showed the importance of heat effects in a photocatalytic reaction. As we keep increasing the external heating to 325 °C, the reaction would ultimately reach to a steady stage, where thermal heating outcompetes the effects of photothermal heating, and the non-thermal effect was also suppressed due to the elevated temperature. The temperature dependence studies on plasmonic NPs for their absorption efficiency showed that as temperature increases from 100 to 700 K, the corresponding absorption efficiency and electric field enhancement decrease.⁵⁹ Since the absorption efficiency is directly related to the polarizability of NPs, the enhanced thermal oscillation can degrade polarizability. Moreover, the increased light intensity would linearly increase the generation of hot electron and the interaction between electron to substrate. But it would quadratically increase the rate of electron hole pair recombination. As a result, the reaction rate would increase linearly as light intensity in the low-intensity region, but it would reach a plateau under high light intensity, since the recombination rate is faster than electron transferring within NP or towards the substrate.⁶⁰⁻⁶² To eliminate the

mass-transfer limit hypothesis, we performed the calculation for reaction quotient. The equilibrium constant of CO₂ methanation decreases when increasing the temperature and is around 1808 (mol/L)² at 400°C.⁶³ The highest reaction quotient observed for our system increased with temperature increase and reached its maximum value of 361 (mol/L)² at 400°C under 1.41 W·cm⁻² (Figure S8a), which is much lower than the literature value. Thus, the reaction is far away from equilibrium under our reaction conditions discussed. Figure S7b shows the conversion of CO₂ and H₂, the H₂ is the limiting agent.

After studying the performance of replacing Rh/TiO₂ to TiN to achieve a higher surface temperature and better production rate under UV and white light. We then want to qualitatively compare the enhanced light effects and their light effectiveness. We previously propose a new index named as overall light effectiveness (OLE), defined as the amount of additional products produced under direct illumination (compare to dark conditions) per second per unit power of light, regardless of catalyst mass (Eq. 2).

$$\text{Overall light effectiveness } (\mu\text{mol}\cdot\text{s}^{-1}/\text{W}\cdot\text{cm}^{-2}) = \frac{\text{Total production rate enhanced by light } (\mu\text{mol}\cdot\text{s}^{-1})}{\text{Light intensity } (\text{W}\cdot\text{cm}^{-2})} \quad (2)$$

OLE is different from apparent quantum efficiency (AQE), where AQE only consider the amount of product generated over the number of photon being absorbed under specific wavelength. However, AQE itself is not sufficient to describe the overall enhancement from light in such a complicated process where both photothermal and non-thermal effects exist and it is difficult to show the photothermal effect using quantum efficiency. Based on the calculations, there are an increased light effectiveness under both UV and white light under 100 °C, and the highest OLE enhancement exist around 1.5 W·cm⁻², and become smaller as light intensity increases (Figure 5a). As we increased the external heating effects to 325°C, 20 mg Rh/TiO₂ achieved an OLE around 0.83 μmol·s⁻¹/W· cm⁻² under UV light at 0.67 W·cm⁻² (Figure 5b). The result is consistence with our previous study. However, Rh/TiO₂:TiN (4:1) shows a better performance under both UV and white light, since there are only 80% of catalyst and generate less product under dark thermal conditions. These results indicate the enhanced photothermal contribution and the importance of the non-thermal effect since the highest OLE is obtained under UV light. Moreover, the enhanced OLE illustrates a more efficient way of catalyst design in combing the photothermal and non-thermal effects together to achieve a better light utilization as well as product generation.

For the broadband solar absorber TiN, it would undergo single light to heat mechanism. When the energy of the incident light is larger than the band gap of the semiconductor, the electrons in the valence band (VB) of the semiconductor are excited to the conduction band (CB) by photons, and the corresponding holes are generated in the VB. The generated electron would eventually return to the lower energy states and release energy in the form of radiative relaxation, emitting photons, or non-radiative relaxation in the form of phonons (heat) by transferring energy to surroundings. When energy is released in the form of phonons, it causes localized heating of the lattice, establishing a temperature distribution that depends on the optical absorption and volume/surface recombination characteristics. The photothermal effect is a consequence of this temperature distribution resulting from the diffusion of optically excited carriers throughout the material and their recombination.⁶⁴ Even though, some reports indicate that TiN exhibits a

plasmonic effect under visible light range.^{56, 65-67} The TiN we used has an averaged particle size of 200-400 nm. As the NP size increases, the plasmon-coupled peak undergoes red-shift and peak broadening, leading to a weaker LSPR effect.⁶⁸⁻⁷⁰ The control experiments show little enhancement for our TiN under white light for photocatalysis. (Fig. S3b). By the same time, the plasmonic photocatalyst Rh/TiO₂ undergo photothermal, hot-electron or non-thermal and external heating effects. Our previous studies quantitatively separate the non-thermal an photothermal effects through different methods.⁴³ For plasmonic nanoparticles, it will undergo LSPR and lead to the generation of hot electrons. The coherent oscillation can be damped by coupling to phonons, resulting in highly efficient photothermal heating at the nanoparticle surface and in its direct surroundings. The environment will subsequently be heated up due to the photoinduced temperature gradient.⁷¹ When Rh/TiO₂ and TiN mixed together, the photothermal effect from TiN would assist and heat up the surrounding even further to achieve a better light absorptivity and overall light enhancement.

CONCLUSION

Overall, this work proposes a new idea in catalysis preparation, by mixing plasmonic photocatalyst with broadband solar absorbers. Our results showed that under milder heating conditions and light illumination, replacing part of the catalyst with solar absorber would not decrease the total production rate, but instead enhance the performance as well as the overall light effectiveness. Thus, highest OLE could always be achieved when we consider enhancing the light absorptivity of catalyst and utilize both photothermal and non-thermal effects. Further research should try other nanocomposites when designing the catalyst and study the performance under solar light illumination where more light can be absorbed.

ASSOCIATED CONTENT

Supporting Information Description

The supporting information includes size distribution and TEM image of Rh NPs; UV-vis spectra of Rh NP, TiO₂, Rh/TiO₂, Rh/TiO₂:TiO₂ (4:1), and emission spectra of UV and White light; XPS studies; selectivity study; reactor setup illustration; thermocatalysis and photocatalysis study for Rh/TiO₂, TiO₂ and TiN; equilibrium study.

AUTHOR INFORMATION

Corresponding Author

Jie Liu – Department of Chemistry, Duke University, Durham, NC 27705, United States;
orcid.org/0000-0003-0451-6111

Email: j.liu@duke.edu

Authors

Zhijia Geng - Department of Chemistry, Duke University, Durham, NC 27705, United States;
orcid.org/0009-0003-3227-6132

Yifan Yu - Department of Chemistry, Duke University, Durham, NC 27705, United States;
orcid.org/0009-0003-0373-4405

Notes

The authors declare no competing financial interest.

ACKNOWLEDGMENTS

This work was supported by a grant from National Science Foundation (grant number CHE-1954838). Some of the characterizations were performed at the Duke University Shared Materials Instrumentation Facility (SMIF), a member of the North Carolina Research Triangle Nanotechnology Network (RTNN), which is supported by the National Science Foundation (award number ECCS-2025064) as part of the National Nanotechnology Coordinated Infrastructure (NNCI).

REFERENCES

(1) Sorrell, S. Reducing energy demand: A review of issues, challenges and approaches. *Renew Sust Energ Rev* **2015**, *47*, 74-82. DOI: 10.1016/j.rser.2015.03.002.

(2) Lakatos, L.; Hevessy, G.; Kovács, J. Advantages and Disadvantages of Solar Energy and Wind-Power Utilization. *World Futures* **2011**, *67* (6), 395-408. DOI: 10.1080/02604020903021776.

(3) Liu, C. X.; Huang, J. F.; Hsiung, C. E.; Tian, Y.; Wang, J. J.; Han, Y.; Fratalocchi, A. High-Performance Large-Scale Solar Steam Generation with Nanolayers of Reusable Biomimetic Nanoparticles. *Adv Sustain Syst* **2017**, *1* (1-2), 1600013. DOI: 10.1002/adssu.201600013.

(4) Jin, H. C.; Lin, G. P.; Bai, L. Z.; Zeiny, A.; Wen, D. S. Steam generation in a nanoparticle-based solar receiver. *Nano Energy* **2016**, *28*, 397-406. DOI: 10.1016/j.nanoen.2016.08.011.

(5) Song, G. F.; Yuan, Y.; Liu, J.; Liu, Q. L.; Zhang, W.; Fang, J.; Gu, J. J.; Ma, D. L.; Zhang, D. Biomimetic Superstructures Assembled from Au Nanostars and Nanospheres for Efficient Solar Evaporation. *Adv Sustain Syst* **2019**, *3* (6), 1900003. DOI: 10.1002/adssu.201900003.

(6) Jin, H. C.; Lin, G. P.; Zeiny, A.; Bai, L. Z.; Wen, D. S. Nanoparticle-based solar vapor generation: An experimental and numerical study. *Energy* **2019**, *178*, 447-459. DOI: 10.1016/j.energy.2019.04.085.

(7) Zhang, H.; Ou, J.; Fang, X.; Lei, S.; Wang, F.; Li, C.; Li, W.; Hu, Y.; Amirfazli, A.; Wang, P. Robust superhydrophobic fabric via UV-accelerated atmospheric deposition of polydopamine and silver nanoparticles for solar evaporation and water/oil separation. *Chemical Engineering Journal* **2022**, *429*, 132539. DOI: 10.1016/j.cej.2021.132539.

(8) Fan, X. F.; Mu, H. C.; Xu, Y. L.; Song, C. W.; Liu, Y. M. Silver nanoparticles-polydopamine-wax gourd: An antimicrobial solar evaporator with enhanced steam generation. *Int J Energ Res* **2022**, *46* (7), 8949-8961. DOI: 10.1002/er.7773.

(9) Meng, S.; Zha, X. J.; Wu, C.; Zhao, X.; Yang, M. B.; Yang, W. Interfacial Radiation-Absorbing Hydrogel Film for Efficient Thermal Utilization on Solar Evaporator Surfaces. *Nano Lett* **2021**, *21* (24), 10516-10524. DOI: 10.1021/acs.nanolett.1c04066.

(10) Ghafurian, M. M.; Niazmand, H.; Goharshadi, E. K.; Zahmatkesh, B. B.; Moallemi, A. E.; Mehrkhah, R.; Mahian, O. Enhanced solar desalination by delignified wood coated with bimetallic Fe/Pd nanoparticles. *Desalination* **2020**, *493*, 114657. DOI: 10.1016/j.desal.2020.114657.

(11) Fan, Y. K.; Wang, S.; Wang, F.; He, J. X.; Tian, Z. Y.; Zhao, H. Y.; Zhu, Z. Q.; Sun, H. X.; Liang, W. D.; Li, A. The assembly of a polymer and metal nanoparticle coated glass capillary array for efficient solar desalination. *J Mater Chem A* **2020**, *8* (48), 25904-25912. DOI: 10.1039/d0ta08950h.

(12) Hamed, M. S. G.; Mola, G. T. Copper sulphide as a mechanism to improve energy harvesting in thin film solar cells. *J Alloy Compd* **2019**, *802*, 252-258. DOI: 10.1016/j.jallcom.2019.06.108.

(13) Liu, P.; Li, X. Y.; Xu, L.; Chen, C.; Yuan, B. L.; Labiad, L.; Hu, Y. B.; Fu, M. L. Recent progress in interfacial photo-vapor conversion technology using metal sulfide-based semiconductor materials. *Desalination* **2022**, *527*, 115532. DOI: 10.1016/j.desal.2021.115532.

(14) Li, W. X.; Jian, H. W.; Wang, W.; Yu, D. Highly efficient solar vapour generation via self-floating three-dimensional Ti_2O_3 -based aerogels. *Colloid Surface A* **2022**, *634*, 128031. DOI: 10.1016/j.colsurfa.2021.128031.

(15) Mergenbayeva, S.; Atabaev, T. S.; Poulopoulos, S. G. $\text{Ti}_2\text{O}_3/\text{TiO}_2$ -Assisted Solar Photocatalytic Degradation of 4-tert-Butylphenol in Water. *Catalysts* **2021**, *11* (11), 1379. DOI: 10.3390/catal11111379.

(16) Zahmatkesh, B. B.; Niazmand, H.; Goharshadi, E. K. Synergistic effect of Fe_3O_4 nanoparticles and Au nanolayer in enhancement of interfacial solar steam generation. *Mater Res Bull* **2023**, *162*, 112178. DOI: 10.1016/j.materresbull.2023.112178.

(17) He, W.; Zhou, L.; Wang, M.; Cao, Y.; Chen, X.; Hou, X. Structure development of carbon-based solar-driven water evaporation systems. *Sci Bull (Beijing)* **2021**, *66* (14), 1472-1483. DOI: 10.1016/j.scib.2021.02.014.

(18) Chen, L.; Wang, H. Y.; Kuravi, S.; Kota, K.; Park, Y. H.; Xu, P. Low-cost and reusable carbon black based solar evaporator for effective water desalination. *Desalination* **2020**, *483*, 114412. DOI: 10.1016/j.desal.2020.114412.

(19) Zhou, X.; Guo, Y.; Zhao, F.; Yu, G. Hydrogels as an Emerging Material Platform for Solar Water Purification. *Acc Chem Res* **2019**, *52* (11), 3244-3253. DOI: 10.1021/acs.accounts.9b00455.

(20) Chen, Q.; Pei, Z.; Xu, Y.; Li, Z.; Yang, Y.; Wei, Y.; Ji, Y. A durable monolithic polymer foam for efficient solar steam generation. *Chem Sci* **2018**, *9* (3), 623-628, 10.1039/C7SC02967E. DOI: 10.1039/c7sc02967e.

(21) Djellabi, R.; Noureen, L.; Dao, V.; Meroni, D.; Falletta, E.; Dionysiou, D. D. D.; Bianchi, C. L. Recent advances and challenges of emerging solar-driven steam and the contribution of photocatalytic effect. *Chemical Engineering Journal* **2022**, *431*, 134024. DOI: 10.1016/j.cej.2021.134024.

(22) Wang, R.; Deng, J. S.; Wu, P.; Ma, Q. L.; Dong, X. T.; Yu, W. S.; Liu, G. X.; Wang, J. X.; Liu, L. Sandwich-type absorber for synergistically enhanced solar water evaporation and photocatalysis. *J Environ Chem Eng* **2022**, *10* (4), 108173. DOI: 10.1016/j.jece.2022.108173.

(23) Guo, M.; Yuan, B.; Sui, Y.; Xiao, Y.; Dong, J.; Yang, L.; Bai, L.; Yang, H.; Wei, D.; Wang, W.; et al. Rational design of molybdenum sulfide/tungsten oxide solar absorber with enhanced photocatalytic degradation toward dye wastewater purification. *J Colloid Interface Sci* **2023**, *631* (Pt B), 33-43. DOI: 10.1016/j.jcis.2022.11.015.

(24) Wang, Z.; Horseman, T.; Straub, A. P.; Yip, N. Y.; Li, D.; Elimelech, M.; Lin, S. Pathways and challenges for efficient solar-thermal desalination. *Sci Adv* **2019**, *5* (7), eaax0763. DOI: 10.1126/sciadv.aax0763.

(25) Osterloh, F. E.; Parkinson, B. A. Recent developments in solar water-splitting photocatalysis. *Mrs Bull* **2011**, *36* (1), 17-22. DOI: 10.1557/mrs.2010.5.

(26) Wei, X.; Zhang, X.; Ali, S.; Wang, J.; Zhou, Y.; Chen, H.; Zhang, G.; Qi, J.; He, D. Carbon intercalated MoS_2 cocatalyst on $\text{g-C}_3\text{N}_4$ photo-absorber for enhanced photocatalytic H_2 evolution under the simulated solar light. *International Journal of Hydrogen Energy* **2023**, *48* (37), 13827-13842. DOI: 10.1016/j.ijhydene.2022.12.257.

(27) Van Hal, A.; Dulski, B.; Postel, A. M. Reduction of CO_2 emissions in houses of historic and visual importance. *Sustainability* **2010**, *2* (2), 443-460. DOI: 10.3390/su2020443.

(28) May, M. M.; Rehfeld, K. Negative Emissions as the New Frontier of Photoelectrochemical CO_2 Reduction. *Adv Energy Mater* **2022**, *12* (21), 2103801. DOI: 10.1002/aenm.202103801.

(29) Edelmannova, M.; Lin, K. Y.; Wu, J. C. S.; Troppova, I.; Capek, L.; Koci, K. Photocatalytic hydrogenation and reduction of CO_2 over CuO/TiO_2 photocatalysts. *Appl Surf Sci* **2018**, *454*, 313-318. DOI: 10.1016/j.apsusc.2018.05.123.

(30) Kamal, K. M.; Narayan, R.; Chandran, N.; Popovic, S.; Nazrulla, M. A.; Kovac, J.; Vrtovec, N.; Bele, M.; Hodnik, N.; Krzmarc, M. M.; et al. Synergistic enhancement of photocatalytic CO₂ reduction by plasmonic Au nanoparticles on TiO₂ decorated N-graphene heterostructure catalyst for high selectivity methane production. *Appl Catal B-Environ* **2022**, *307*, 121181. DOI: 10.1016/j.apcatb.2022.121181.

(31) Mazierski, P.; Mikolajczyk, A.; Bajorowicz, B.; Malankowska, A.; Zaleska-Medynska, A.; Nadolna, J. The role of lanthanides in TiO₂-based photocatalysis: A review. *Appl Catal B-Environ* **2018**, *233*, 301-317. DOI: 10.1016/j.apcatb.2018.0.4.019.

(32) Tan, T. H.; Scott, J.; Ng, Y. H.; Taylor, R. A.; Aguey-Zinsou, K. F.; Amal, R. Understanding Plasmon and Band Gap Photoexcitation Effects on the Thermal-Catalytic Oxidation of Ethanol by TiO₂-Supported Gold. *Acs Catal* **2016**, *6* (3), 1870-1879. DOI: 10.1021/acscatal.5b02785.

(33) Cortes, E. Activating plasmonic chemistry. *Science* **2018**, *362* (6410), 28-29. DOI: 10.1126/science.aav1133.

(34) Zhou, L.; Swearer, D. F.; Zhang, C.; Robatjazi, H.; Zhao, H.; Henderson, L.; Dong, L.; Christopher, P.; Carter, E. A.; Nordlander, P.; et al. Quantifying hot carrier and thermal contributions in plasmonic photocatalysis. *Science* **2018**, *362* (6410), 69-72. DOI: 10.1126/science.aat6967.

(35) Szczerbinski, J.; Metternich, J. B.; Goubert, G.; Zenobi, R. How Peptides Dissociate in Plasmonic Hot Spots. *Small* **2020**, *16* (4), e1905197. DOI: 10.1002/smll.201905197.

(36) Jovic, V.; Chen, W.-T.; Sun-Waterhouse, D.; Blackford, M. G.; Idriss, H.; Waterhouse, G. I. N. Effect of gold loading and TiO₂ support composition on the activity of Au/TiO₂ photocatalysts for H₂ production from ethanol–water mixtures. *Journal of Catalysis* **2013**, *305*, 307-317. DOI: 10.1016/j.jcat.2013.05.031.

(37) Tallósy, S. P.; Janovák, L.; Ménesi, J.; Nagy, E.; Juhász, Á.; Balázs, L.; Deme, I.; Buzás, N.; Dékány, I. Investigation of the antibacterial effects of silver-modified TiO₂ and ZnO plasmonic photocatalysts embedded in polymer thin films. *Environmental Science and Pollution Research* **2014**, *21* (19), 11155-11167. DOI: 10.1007/s11356-014-2568-6.

(38) Hong, D. C.; Lyu, L. M.; Koga, K.; Shimoyama, Y.; Kon, Y. Plasmonic Ag@TiO₂ Core-Shell Nanoparticles for Enhanced CO₂ Photoconversion to CH₄. *Acs Sustain Chem Eng* **2019**, *7* (23), 18955-18964. DOI: 10.1021/acssuschemeng.9b04345.

(39) Yao, G. Y.; Zhao, Z. Y.; Liu, Q. L.; Dong, X. D.; Zhao, Q. M. Theoretical calculations for localized surface plasmon resonance effects of Cu/TiO₂ nanosphere: Generation, modulation, and application in photocatalysis. *Sol Energ Mat Sol C* **2020**, *208*, 110385. DOI: 10.1016/j.solmat.2019.110385.

(40) Esmat, M.; Doustkhah, E.; Abdelbar, M.; Tahawy, R.; El-Hosainy, H.; Abdelhameed, M.; Ide, Y.; Fukata, N. Structural Conversion of Cu-Titanate into Photoactive Plasmonic Cu-TiO₂ for H₂ Generation in Visible Light. *Acs Sustain Chem Eng* **2022**, *10* (13), 4143-4151. DOI: 10.1021/acssuschemeng.1c07555.

(41) Bayles, A.; Tian, S.; Zhou, J.; Yuan, L.; Yuan, Y.; Jacobson, C. R.; Farr, C.; Zhang, M.; Swearer, D. F.; Solti, D. Al@TiO₂ Core–shell nanoparticles for plasmonic photocatalysis. *ACS nano* **2022**, *16* (4), 5839-5850. DOI: 10.1021/acsnano.1c10995.

(42) Liu, J.; Xu, M.; Zhang, T.; Chu, X.; Shi, K.; Li, J. Al/TiO₂ composite as a photocatalyst for the degradation of organic pollutants. *Environ Sci Pollut Res Int* **2023**, *30* (4), 9738-9748. DOI: 10.1007/s11356-022-22861-9.

(43) Li, X. Q.; Everitt, H. O.; Liu, J. Confirming nonthermal plasmonic effects enhance CO₂ methanation on Rh/TiO₂ catalysts. *Nano Res* **2019**, *12* (8), 1906-1911. DOI: 10.1007/s12274-019-2457-x.

(44) Li, X. Q.; Everitt, H. O.; Liu, J. Synergy between thermal and nonthermal effects in plasmonic photocatalysis. *Nano Res* **2020**, *13* (5), 1268-1280. DOI: 10.1007/s12274-020-2694-z.

(45) Karelovic, A.; Ruiz, P. Mechanistic study of low temperature CO₂ methanation over Rh/TiO₂ catalysts. *Journal of Catalysis* **2013**, *301*, 141-153. DOI: 10.1016/j.jcat.2013.02.009.

(46) Yang, Y. J.; Liu, J.; Liu, F.; Wu, D. W. Reaction mechanism of CO₂ methanation over Rh/TiO₂ catalyst. *Fuel* **2020**, *276*, 118093. DOI: 10.1016/j.fuel.2020.118093.

(47) Cortes, E.; Besteiro, L. V.; Alabastri, A.; Baldi, A.; Tagliabue, G.; Demetriadou, A.; Narang, P. Challenges in Plasmonic Catalysis. *ACS Nano* **2020**, *14* (12), 16202-16219. DOI: 10.1021/acsnano.0c08773.

(48) Li, X.; Zhang, X.; Everitt, H. O.; Liu, J. Light-Induced Thermal Gradients in Ruthenium Catalysts Significantly Enhance Ammonia Production. *Nano Lett* **2019**, *19* (3), 1706-1711. DOI: 10.1021/acs.nanolett.8b04706.

(49) Zhang, Z.; Zhang, C.; Zheng, H.; Xu, H. Plasmon-Driven Catalysis on Molecules and Nanomaterials. *Acc Chem Res* **2019**, *52* (9), 2506-2515. DOI: 10.1021/acs.accounts.9b00224.

(50) Li, R. G.; Cheng, W. H.; Richter, M. H.; DuChene, J. S.; Tian, W. M.; Li, C.; Atwater, H. A. Unassisted Highly Selective Gas-Phase CO₂ Reduction with a Plasmonic Au/p-GaN Photocatalyst Using H₂O as an Electron Donor. *Acs Energy Lett* **2021**, *6* (5), 1849-1856. DOI: 10.1021/acsenergylett.1c00392.

(51) Veziroglu, S.; Ullrich, M.; Hussain, M.; Drewes, J.; Shondo, J.; Strunskus, T.; Adam, J.; Faupel, F.; Aktas, O. C. Plasmonic and non-plasmonic contributions on photocatalytic activity of Au-TiO₂ thin film under mixed UV-visible light. *Surf Coat Tech* **2020**, *389*, 125613. DOI: 10.1016/j.surfcoat.2020.125613.

(52) Dubi, Y.; Un, I. W.; Baraban, J. H.; Sivan, Y. Distinguishing thermal from non-thermal contributions to plasmonic hydrodefluorination. *Nat Catal* **2022**, *5* (4), 244-246. DOI: 10.1038/s41929-022-00767-6.

(53) Zhang, X.; Li, X.; Reish, M. E.; Zhang, D.; Su, N. Q.; Gutiérrez, Y.; Moreno, F.; Yang, W.; Everitt, H. O.; Liu, J. Plasmon-enhanced catalysis: distinguishing thermal and nonthermal effects. *Nano letters* **2018**, *18* (3), 1714-1723. DOI: 10.1021/acs.nanolett.7b04776.

(54) Lovell, E. C.; Scott, J.; Bedford, N. M.; Tan, T. H.; Cullen, P. J.; Ostrikov, K. K.; Amal, R. Two Steps Back, One Leap Forward: Synergistic Energy Conversion in Plasmonic and Plasma Catalysis. *Acs Energy Lett* **2021**, *7* (1), 300-309. DOI: 10.1021/acsenergylett.1c02387.

(55) Han, S.; Shin, J. H.; Jung, P. H.; Lee, H.; Lee, B. J. Broadband Solar Thermal Absorber Based on Optical Metamaterials for High-Temperature Applications. *Adv Opt Mater* **2016**, *4* (8), 1265-1273. DOI: 10.1002/adom.201600236.

(56) Patsalas, P.; Kalfagiannis, N.; Kassavetis, S. Optical Properties and Plasmonic Performance of Titanium Nitride. *Materials* **2015**, *8* (6), 3128-3154. DOI: 10.3390/ma8063128.

(57) Yu, M. J.; Chang, C. L.; Lan, H. Y.; Chiao, Z. Y.; Chen, Y. C.; Lee, H. W. H.; Chang, Y. C.; Chang, S. W.; Tanaka, T.; Tung, V.; et al. Plasmon-Enhanced Solar-Driven Hydrogen Evolution Using Titanium Nitride Metasurface Broadband Absorbers. *Acs Photonics* **2021**, *8* (11), 3125-3132. DOI: 10.1021/acspophotonics.1c00927.

(58) Watson, A. M.; Zhang, X.; Alcaraz de la Osa, R.; Marcos Sanz, J.; Gonzalez, F.; Moreno, F.; Finkelstein, G.; Liu, J.; Everitt, H. O. Rhodium nanoparticles for ultraviolet plasmonics. *Nano Lett* **2015**, *15* (2), 1095-1100. DOI: 10.1021/nl5040623.

(59) He, W. M.; Huang, X.; Ma, X. C.; Zhang, J. Q. Significant temperature effect on the LSPR properties of noble metal nanoparticles. *J Opt-India* **2022**, *51* (1), 142-153. DOI: 10.1007/s12596-021-00766-z.

(60) Sun, J. P.; Ren, Y. T.; Gao, R. X.; Gao, B. H.; He, M. J.; Qi, H. Influence of the temperature-dependent dielectric constant on the photoacoustic effect of gold nanospheres. *Phys Chem Chem Phys* **2022**, *24* (48), 29667-29682, 10.1039/D2CP03866H. DOI: 10.1039/d2cp03866h.

(61) Thrall, E. S.; Steinberg, A. P.; Wu, X. M.; Brus, L. E. The Role of Photon Energy and Semiconductor Substrate in the Plasmon-Mediated Photooxidation of Citrate by Silver Nanoparticles. *J Phys Chem C* **2013**, *117* (49), 26238-26247. DOI: 10.1021/jp409586z.

(62) Kim, Y.; Smith, J. G.; Jain, P. K. Harvesting multiple electron-hole pairs generated through plasmonic excitation of Au nanoparticles. *Nat Chem* **2018**, *10* (7), 763-769. DOI: 10.1038/s41557-018-0054-3.

(63) Gao, J.; Liu, Q.; Gu, F.; Liu, B.; Zhong, Z.; Su, F. Recent advances in methanation catalysts for the production of synthetic natural gas. *Rsc Advances* **2015**, *5* (29), 22759-22776. DOI: 10.1039/C4RA16114A.

(64) Li, J.; Zhang, W.; Ji, W.; Wang, J.; Wang, N.; Wu, W.; Wu, Q.; Hou, X.; Hu, W.; Li, L. Near infrared photothermal conversion materials: mechanism, preparation, and photothermal cancer therapy applications. *J Mater Chem B* **2021**, *9* (38), 7909-7926. DOI: 10.1039/d1tb01310f.

(65) Shah, D.; Catellani, A.; Reddy, H.; Kinsey, N.; Shalaev, V.; Boltasseva, A.; Calzolari, A. Controlling the Plasmonic Properties of Ultrathin TiN Films at the Atomic Level. *Acs Photonics* **2018**, *5* (7), 2816-2824. DOI: 10.1021/acspophotonics.7b01553.

(66) Rej, S.; Mascaretti, L.; Santiago, E. Y.; Tomanec, O. e.; Kment, S. t. p. n.; Wang, Z.; Zbořil, R.; Fornasiero, P.; Govorov, A. O.; Naldoni, A. Determining plasmonic hot electrons and photothermal effects during H₂ evolution with TiN–Pt nanohybrids. *Acs Catal* **2020**, *10* (9), 5261-5271. DOI: 10.1021/acscatal.0c00343.

(67) Popov, A. A.; Tselikov, G.; Dumas, N.; Berard, C.; Metwally, K.; Jones, N.; Al-Kattan, A.; Larrat, B.; Braguer, D.; Mensah, S.; et al. Laser- synthesized TiN nanoparticles as promising plasmonic alternative for biomedical applications. *Sci Rep* **2019**, *9* (1), 1194. DOI: 10.1038/s41598-018-37519-1.

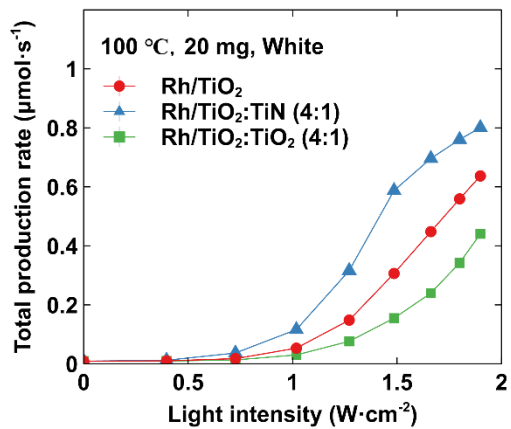
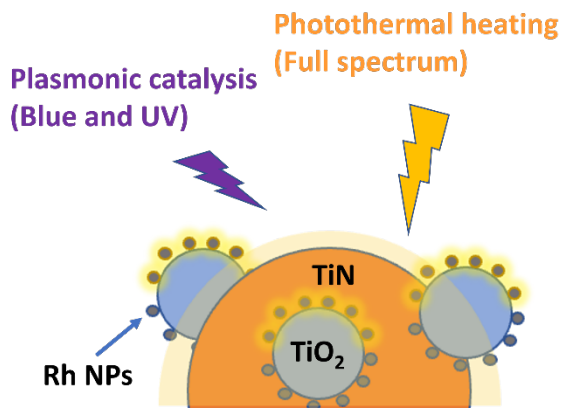
(68) Bonin, G. O.; Barrow, S. J.; Connell, T. U.; Roberts, A.; Chesman, A. S. R.; Gomez, D. E. Self-Assembly of Plasmonic Near-Perfect Absorbers of Light: The Effect of Particle Size. *J Phys Chem Lett* **2020**, *11* (19), 8378-8385. DOI: 10.1021/acs.jpclett.0c02461.

(69) Kinnan, M. K.; Chumanov, G. Plasmon Coupling in Two-Dimensional Arrays of Silver Nanoparticles: II. Effect of the Particle Size and Interparticle Distance. *J Phys Chem C* **2010**, *114* (16), 7496-7501. DOI: 10.1021/jp911411x.

(70) Naldoni, A.; Guler, U.; Wang, Z. X.; Marelli, M.; Malara, F.; Meng, X. G.; Besteiro, L. V.; Govorov, A. O.; Kildishev, A. V.; Boltasseva, A.; et al. Broadband Hot-Electron Collection for Solar Water Splitting with Plasmonic Titanium Nitride. *Adv Opt Mater* **2017**, *5* (15), 1601031. DOI: 10.1002/adom.201601031.

(71) Baffou, G.; Bordacchini, I.; Baldi, A.; Quidant, R. Simple experimental procedures to distinguish photothermal from hot-carrier processes in plasmonics. *Light Sci Appl* **2020**, *9* (1), 108. DOI: 10.1038/s41377-020-00345-0.

TOC Graphic



Tables of Contents Image

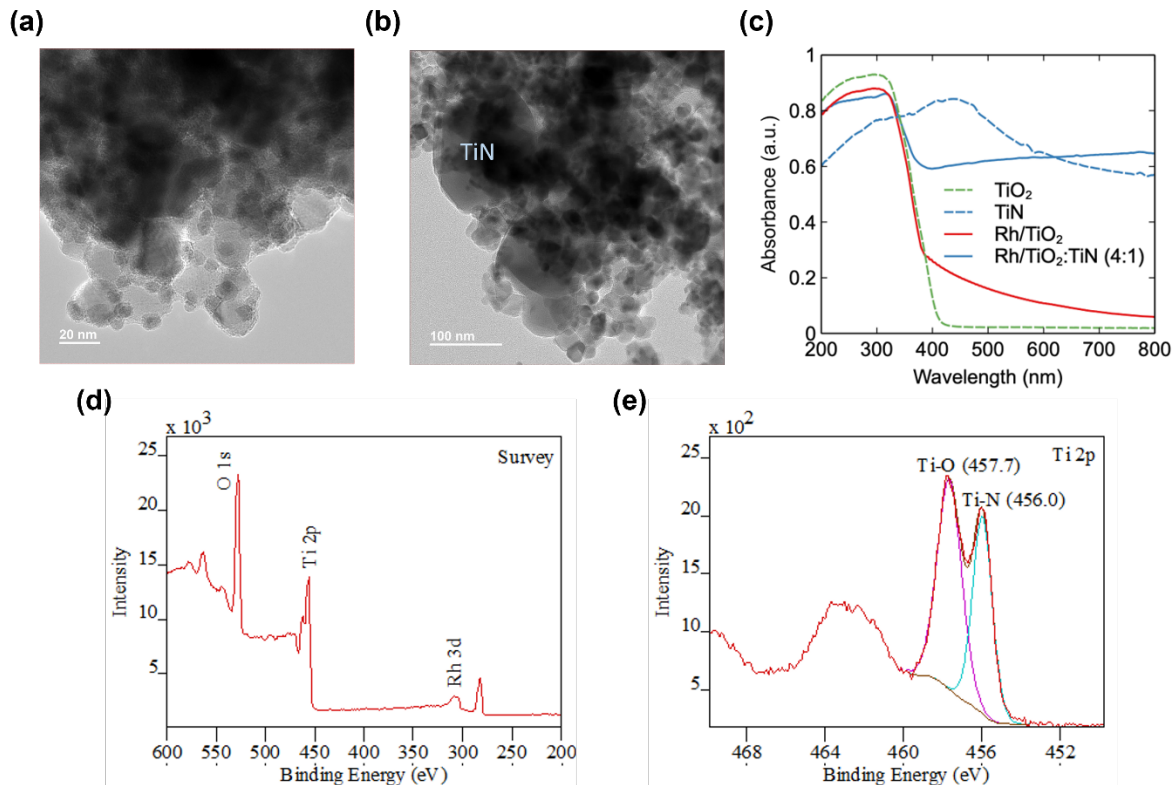


Figure 1. TEM characterization of (a) Rh/TiO₂, scale bar at 20 nm and (b) Rh/TiO₂:TiN (4:1), scale bar at 100nm. (c) UV-vis absorption spectra for TiO₂ (green dash line), TiN (blue dash line), Rh/TiO₂ (red solid line), and Rh/TiO₂:TiN (4:1) (blue solid line). XPS spectra of Rh/TiO₂:TiN (4:1).(d) Survey spectra; (e) high-resolution Ti 2p spectra.

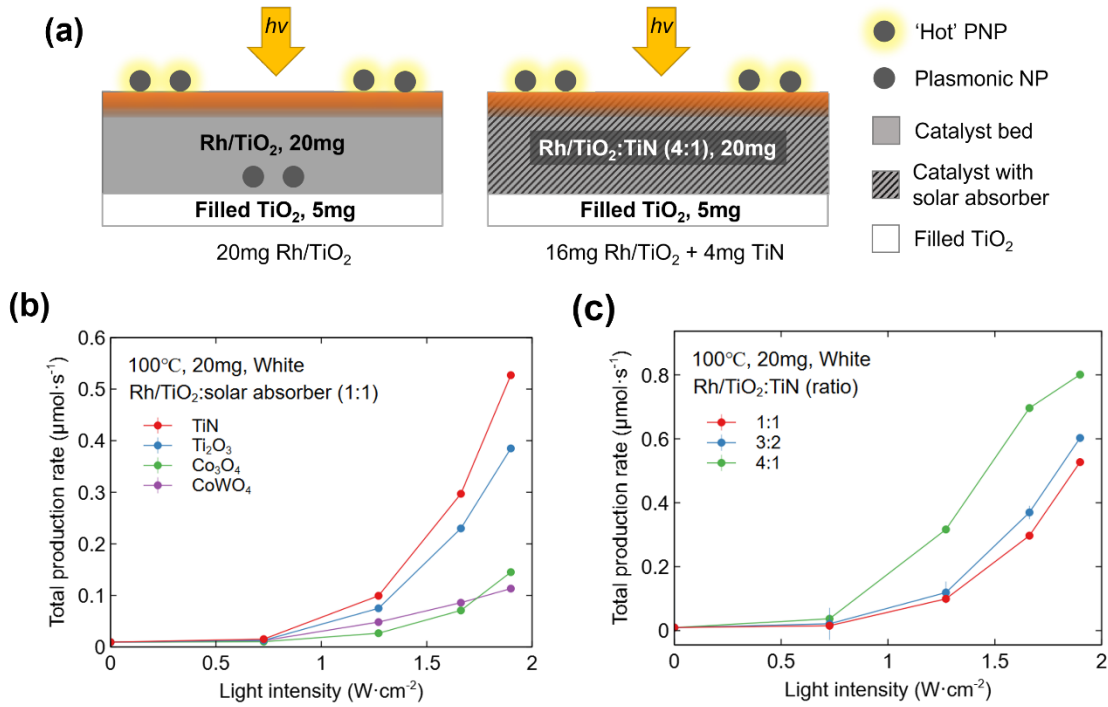


Figure 2. (a) Catalyst bed setup illustrations for both 20 mg Rh/TiO₂ and Rh/TiO₂:TiN (4:1) with filled 5 mg TiO₂ at the bottom. Study the catalytic performance of catalyst mixed with (b) different solar absorbers with 1:1 ratio by mass; (c) TiN at different ratio by mass under 100 °C heating with white light.

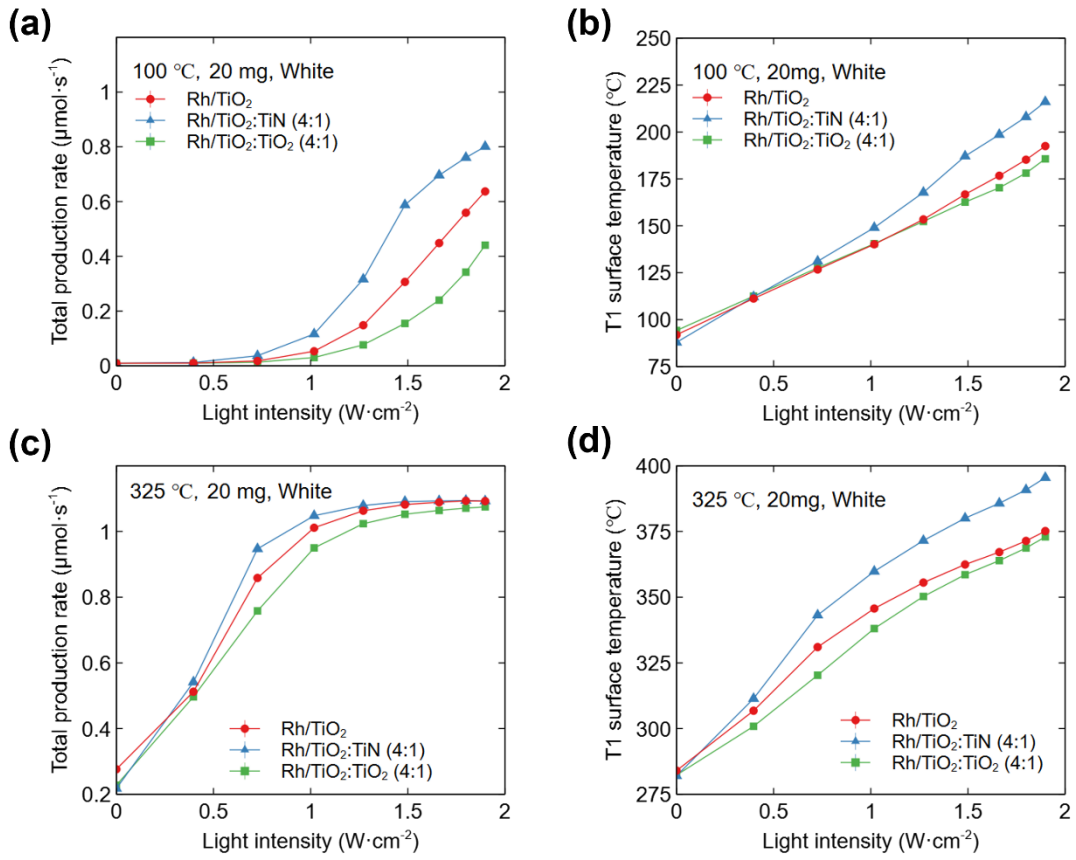


Figure 3. The total production rate and measured surface temperature as a relationship with light intensity for 20 mg of Rh/TiO₂ (red circle), Rh/TiO₂:TiN (4:1, blue triangle), and Rh/TiO₂:TiO₂ (4:1, green square) at (a, b) 100 °C, and (c, d) 325 °C under white light illumination.

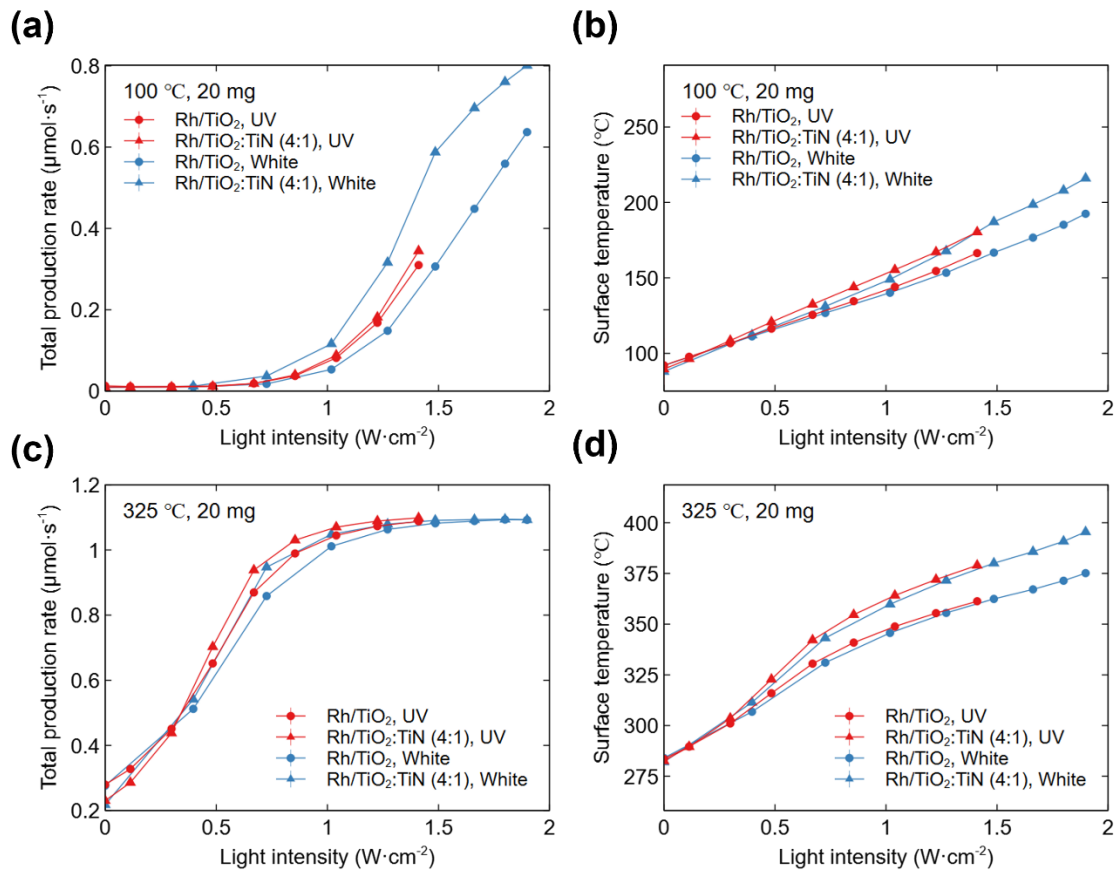


Figure 4. The total production rate, and measured surface temperature as a relationship with light intensity for 20 mg of Rh/TiO₂ (circle), Rh/TiO₂:TiN (4:1, triangle) at (a, b) $100\text{ }^\circ\text{C}$, and (c, d) $325\text{ }^\circ\text{C}$ as a comparison between UV (red) and white light (blue).

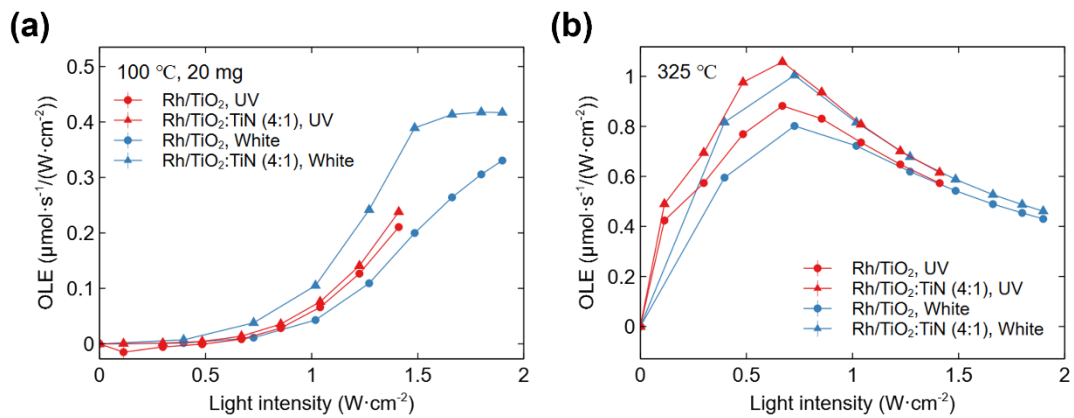


Figure 5. Calculated overall light effectiveness as a relationship with light intensity for 20 mg of Rh/TiO₂ (circle), Rh/TiO₂:TiN (4:1, triangle) at (a) 100 °C, and (b) 325 °C as a comparison between UV (red) and white light (blue).